Chinese Chemical Letters 35 (2024) 109767

Contents lists available at ScienceDirect

Chinese Chemical Letters

journal homepage: www.elsevier.com/locate/cclet

Rationally designed S-scheme heterojunction of BiOCl/g-C_3N_4 for photodegradation of sulfamerazine: Mechanism insights, degradation pathways and DFT calculation

Chunyan Yang[a,b], Qiuyu Rong[a], Fengyin Shi[a], Menghan Cao[a], Guie Li[a], Yanjun Xin[a], Wen Zhang[c], Guangshan Zhang[a,*]

[a] Qingdao Engineering Research Center for Rural Environment, College of Resources and Environment, Qingdao Agricultural University, Qingdao 266109, China
[b] College of Architecture and Environment, Institute of New Energy and Low-Carbon Technology, Sichuan University, Chengdu 610207, China
[c] John A. Reif, sdJr. Department of Civil and Environmental Engineering, New Jersey Institute of Technology, Newark, NJ 07102, United States

ARTICLE INFO

Article history:
Received 2 December 2023
Revised 26 February 2024
Accepted 12 March 2024
Available online 13 March 2024

Keywords:
BiOCl/g-C_3N_4
Visible-light
DFT
Sulfamerazine
Degradation pathways

ABSTRACT

Antibiotics present in surface water have detrimental effects on both human health and the ecosystem. Additionally, they pose a threat to the effectiveness of biological water treatment processes. In this study, a visible photocatalytic system with BiOCl/g-C_3N_4 heterojunction was developed to remove sulfonamide antibiotic sulfamerazine (SMZ) in water. The removal rate reached 92.77% under visible light irradiation for 80 min. This photocatalyst remained active after 5 cycles of experiments and maintained a relatively stable removal rate of SMZ of over 80%. The ESR tests indicate that the main active species in this photocatalytic system were h^+ and $^{\bullet}O_2^-$. The enhanced photocatalytic efficiency was mainly ascribed to the formation of a built-in electric field between BiOCl and g-C_3N_4 through the carrier transport mechanism of the S-scheme heterojunction. This heterojunction facilitated the photogenerated carrier shift and segregation, and improved the interfacial charge transfer efficiency, as confirmed by photoelectrochemical test and Density functional theory (DFT) calculations. The HPLC-QTOF-MS/MS and DFT analysis revealed possible degradation pathways of SMZ may involve deamination, hydroxylation, SO_2 extrusion and bond breaking. This novel BiOCl/g-C_3N_4 heterojunction has proven to be essential for efficient visible-light photocatalysis.

Approximately 100,000–200,000 tons of antibiotics are manufactured globally every year to cure microbial infections in humans and animals, or as feed additives to promote the growth of livestock [1–3]. Sulfamerazine (SMZ), a typical synthetic broad-spectrum antibiotic, is one of the most effective antimicrobial agents in the sulfonamide antibiotic class [4]. The concentration of this substance has been detected worldwide in various environmental matrices, including rivers, soils, sediments, groundwater, treated municipal wastewater, and even drinking water, spanning a range from ng/L to μg/L [5,6]. Accumulation of antibiotics in the environment can lead to increased bacterial resistance and resistance genes [7,8]. More importantly, the transfer of antibiotics through the food chain has the potential to reduce the effectiveness on humans in the near future [9]. In addition, it exhibits toxicity to aquatic organisms, impacts the fertility of specific animal species, and has the potential to disrupt the human endocrine system [10]. Unfortunately, residual SMZ persisting in the environment displays limited biodegradability and is only partially removed by conventional wastewater treatment methods. Therefore, it is crucial to find an effective method to remove this type of sulfonamide antibiotics from the environment to protect ecosystems and human health. Various techniques have been reported for the removal of SMZ from water based on biological, chemical, photochemical, physical adsorption or Fenton methods [3,11,12]. Many of these methods continue to face challenges such as low degradation efficiency, elevated processing costs, incomplete product degradation, and limited practical adoption. Thus, it is of utmost practical significance to discover an efficient and reliable approach for the effective removal of SMZ from wastewater.

Photocatalytic oxidation is a commonly employed method for wastewater pollutant removal, renowned for its environmental friendliness, high efficiency, and cost-effectiveness [13,14]. Many semiconductors including TiO_2, ZnS, ZnO, and CdS have been used

* Corresponding author.
E-mail address: gszhang@qau.edu.cn (G. Zhang).

https://doi.org/10.1016/j.cclet.2024.109767
1001-8417/

as photocatalysts for the treatment of antibiotics [15,16]. Bi-based photocatalysts, in the general form of BiOX (X = Cl, Br, I), have attracted the attention because of their unique layered structure [17], which could generate a strong internal electrostatic field within the crystal and enhance the separation and transfer of photogenerated charges. For example, BiOCl nanosheets with two-dimensional structures yield a large specific surface area, plenty of surface active sites, and effective charge separation and migration efficiency [18,19]. BiOX has been reported in some water purification and environmental restoration such as photocatalytic degradation of organic matter, Cr(VI) removal and CO_2 photoreduction [20,21]. However, the substantial width of the intrinsic BiOCl energy band (~3.3 eV) limits its absorption of UV light and makes it challenging to exhibit visible photocatalytic activity. Therefore, researchers have employed various techniques to augment their capacity for visible light absorption and enhance their photocatalytic performance. These techniques include elemental/ionic group doping, noble metal deposition, morphology manipulation, and the formation of complexes/heterojunctions [22–24]. Among them, the construction of heterojunction serves as a classical strategy to modulate the visible light absorption range of catalysts [25], including two-dimensional ultrathin photocatalysts. For example, the absorption edge of g-C_3N_4, an n-type semiconductor, is about 460 nm and the conduction and valence bands are located at −1.3 eV and 1.4 eV, respectively, which results in the band gap of about 2.7 eV for g-C_3N_4 and enables visible light absorbance [26,27]. Furthermore, Zhao *et al.* [28] prepared a double Z-type heterojunction of ternary $BiVO_4$/g-C_3N_4/$NiFe_2O_4$, and the photocatalytic degradation of ofloxacin by these ternary composites showed rate constants were 3.8, 16.3, and 71.2 times higher than those of $BiVO_4$, g-C_3N_4, and $NiFe_2O_4$, respectively. The novel atomic-scale heterojunction of g-C_3N_4/Bi_2WO_6 was constructed *via* a hydrothermal reaction and elicited a high photogenerated carrier separation efficiency [29]. Under visible-light irradiation, the removal of ibuprofen by g-C_3N_4/Bi_2WO_6 reached nearly 96.1% in 1 h, which was almost 2.7 times higher than that of Bi_2WO_6. The high photocatalytic activity of g-C_3N_4/Bi_2WO_6 was attributed to the synergistic effect of the heterojunctions that promoted photo-induced charge separation. Wang *et al.* [30] prepared tubular g-C_3N_4 (TCN)/BiOI S-scheme heterojunction and achieved the removal rate of more than 77% and 90% for tetracycline (TC) and Cr(VI) within 10 min and 30 min, respectively, under visible light irradiation.

Though the BiOCl/g-C_3N_4 nanocomposites have been reported to yield similar high visible photocatalytic properties [31,32], the preparation methods are relatively tedious and the photocatalytic mechanisms of BiOCl/g-C_3N_4 heterojunctions remain elusive. This study demonstrated a one-step direct precipitation method for the synthesis of an S-scheme BiOCl/g-C_3N_4 heterojunctions and evaluation of visible photocatalytic degradation of SMZ. The effects of reaction conditions, such as catalysts dosage and pH, on the photocatalytic properties were systematically evaluated. The catalyst reusability was evaluated. The main active species of the photocatalytic system were identified by EPR and scavenger experiments. The formation of BiOCl/g-C_3N_4 heterojunctions was further analyzed by photoelectrochemical test and DFT calculations.

In this research, sodium hydroxide (NaOH), hydrochloride (HCl), bismuth nitrate pentahydrate ($Bi(NO_3)_3{\cdot}5H_2O$), urea (H_2NCONH_2), ethylene glycol ($HOCH_2CH_2OH$), thiourea (CH_4N_2S), potassium chloride (KCl), acetic acid (CH_3COOH), anhydrous ethanol (C_2H_5OH), potassium iodide (KI), isopropyl alcohol ($(CH_3)_2CHOH$), *p*-benzoquinone ($C_6H_4O_2$), disodium ethylenediaminetetraacetate ($C_{10}H_{14}N_2O_8Na_2{\cdot}2H_2O$) were all purchased from Tianjin Chemical (China). The water used in the experiments was deionized (DI) water produced by Milli-Q integral water purification systems.

The BiOCl catalyst was prepared by direct precipitation method [33]. Specifically, 1.940 g of $Bi(NO_3)_3{\cdot}5H_2O$ was dissolved in 20 mL of HCl (1.5 mol/L) to obtain solution A. Then, solution A was added dropwise to 10 mL of NaOH solution (0.72 mol/L) under constant stirring, which produced white solid with obvious stratification. After 10 min of stirring, the precipitate was filtered by 0.22-μm mixed cellulose ester membrane filters and washed several times with deionized water. Finally, the resulting solid was dried in an oven at 80 °C for 4 h to obtain the white BiOCl powders. g-C_3N_4 was prepared by thermal polycondensation [34]. Firstly, 30 g of urea was placed in a tubular calciner and calcined at 550 °C with a heating rate of 5 °C/min in an air atmosphere for 4 h. Then the calcined product was dispersed in deionized water with ultrasonication (40 Hz and 100 Watt) for 30 min, and finally washed by DI water for three times with centrifugation. The final obtained solid was dried at 70 °C to obtain light yellow g-C_3N_4 powders. BiOCl/g-C_3N_4 heterojunction was fabricated by *in situ* growth of BiOCl on mesoporous g-C_3N_4 nanoflakes using a one-pot method. Firstly, 0.184 g of g-C_3N_4 powders were added to the mixture of ethylene glycol/deionized water (200 mL, 1:1 (v/v)) and stirred for 10 min. Secondly, an amount of $Bi(NO_3)_3{\cdot}5H_2O$ was added and stirred for another 10 min. Then, 20 mL (1 mol/L) of thiourea was added and stirred continuously for 10 min before adding KCl at the same amount of $Bi(NO_3)_3{\cdot}5H_2O$. Finally, 100 mL of acetic acid (0.35 mol/L) was added and stirred for 1 h. After filtration, the product was washed with water and ethanol three times, respectively. Dried at 100 °C to obtain the pale yellow BiOCl/g-C_3N_4 composite.

The crystal structure of the catalyst was examined by X-ray diffraction (XRD; D/max-III B, Rigaku). The surface micromorphology of the catalysts was investigated by scanning electron microscopy (SEM; Sigma 500, Zeiss, Germany). The surface functional groups of the catalysts were observed by Fourier transform infrared spectrometer (FTIR; Spectrum One, PerkinElmer, USA). The dissolved concentration of Bi^{3+} during the photocatalytic reaction was detected by an inductively coupled plasma atomic emission spectrometer (ICP-AES, Optima 5300DV, Perkin Elmer). An electrochemical workstation (CHI660E, Shanghai Chenhua Instrument Co., China) was applied to test the photoelectrochemical performances of the samples. The light source was a 300W-Xe lamp. An X-ray photoelectron spectroscopy (XPS; Thermo Scientific K-Alpha, USA) was used to analyze chemical composition and chemical states of the samples. The specific surface areas of the catalysts were tested by a Brunauer-Emmett-Teller (BET; Quantachrome Nova 2000e, USA). The optical properties of the catalysts were measured by UV–vis diffuse reflectance spectroscopy (UV–vis DRS; UV-2550, Shimadzu, Japan). The concentration of SMZ was detected by high-performance liquid chromatography (HPLC, Agilent 1260) with a diode array detector (DAD). The injection volume was 10 μL, and the C18 column (5 μm, 4.6 × 250 mm) was employed for detection. Acetonitrile and water flowed at a rate of 0.1 mL/min (60/40, v/v). The detecting wavelength was set as 270 nm [11]. The degradation products of SMZ were detected by HPLC-QTOF-MS/MS (ESI^+, QTOF 6550, Agilent). The electron spin resonance (ESR) signal of the active species generated in the photocatalytic system was detected using an electron spin resonance spectrometer. The total organic carbon (TOC) of SMZ solution the before and after the photocatalytic reaction was mesuresd by a Jena Multi N/C 3100 carbon analyzer.

In the photocatalytic experiment, 0.04 g of BiOCl/g-C_3N_4 composite catalysts were added into 100 mL of 10 mg/L SMZ solution and sonicated for 30 s for mixing. Then, the suspension was placed into a photochemical chamber (CEL-LB70, China) in the dark for 30 min until the adsorption and desorption equilibrium. The Xenon lamp light irradiation was turned on at an intensity of 27.1 mW/cm^2. The concentration of SMZ in the suspension was measured by HPLC after extraction and filtration of the liquid samples from the suspension using a disposable syringe and filter

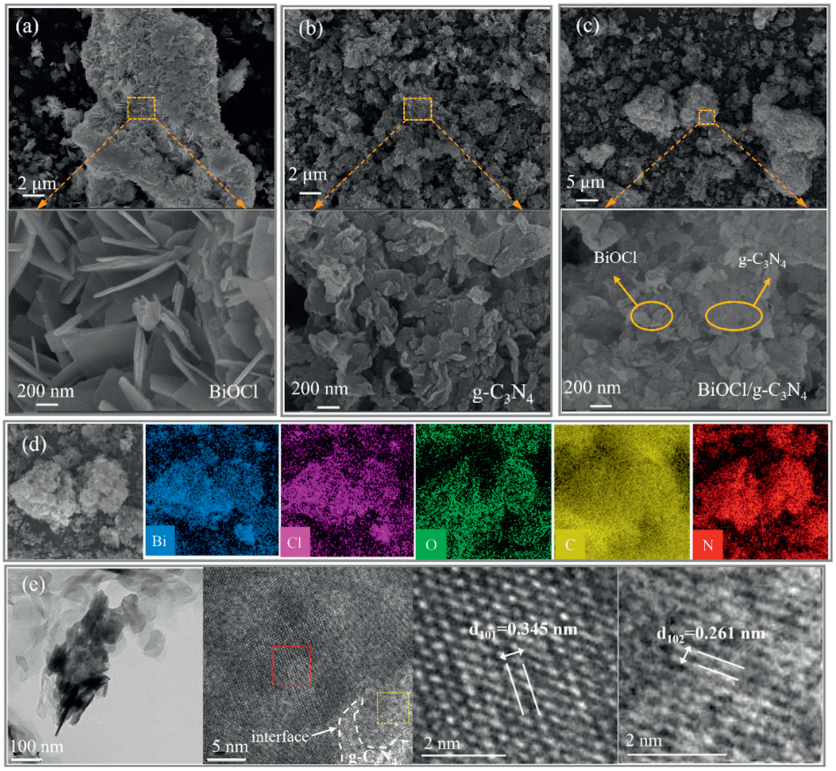

Fig. 1. SEM images of (a) BiOCl, (b) g-C_3N_4 and (c) BiOCl/g-C_3N_4 samples. (d) EDS-Mapping and (e) HRTEM of BiOCl/g-C_3N_4.

(13 mm × 0.22 μm, mixed cellulose ester membrane). After photocatalytic degradation experiments, the catalysts were recovered by filtration, washing with anhydrous ethanol and deionized water. The recovered catalyst was reused in the photocatalytic degradation experiments with the same experimental procedure as above.

DFT calculations including Mulliken populations and Fukui functions were performed by Materials Studio (MS) software to explore the degradation pathways of SMZ. Mulliken populations were calculated to explore the difficulty of breaking chemical bonds in molecules. Meanwhile, the Fukui index represents the probability of an atom being attacked by nucleophilic, electrophilic or free radicals and estimates the active site of each molecule. In this case, the Mulliken population was calculated using the CASTEP module and the Fukui index was calculated using the DMol3 module. To further analyze the photocatalytic mechanism of heterojunctions, DFT calculations were also performed to explore the electronic structures of BiOCl and g-C_3N_4 photocatalysts. The exchange–correlation function was set as Perdew-Burke-Ernzerhof (PBE) and generalized gradient approximation (GGA) [35,36].

As seen in Fig. 1a, BiOCl is a layered structure composed of nanosheets. Fig. 1b shows that the g-C_3N_4 sample displayed a typical two-dimensional lamellar structure, which is aggregated graphite-like, sparsely porous and irregularly shaped [37]. As presented in Fig. 1c, the BiOCl/g-C_3N_4 sample had a layered nanosheet structure. After BiOCl hybridized with g-C_3N_4, nucleation growth of BiOCl took place along the inner face of g-C_3N_4 and formed a heterojunction. From the EDS mapping elemental distribution map (Fig. 1d), it can be observed that the elements Bi, O, Cl, C and N are relatively uniformly distributed on the surface of the BiOCl/g-C_3N_4 composite photocatalysts, which further verifies the successful synthesis of the composite photocatalysts of the BiOCl/g-C_3N_4 composite catalysts. Fig. 1e exhibited the lattice spacings were approximately 0.345 nm and 0.261 nm, which attributed to the spacing of the (101) and (102) planes of orthorhombic BiOCl, while no fringes of g-C_3N_4 were observed due to its disordered state. In addition, the formation of an interface between BiOCl and the g-C_3N_4 layer was also observed, indicating the strong interfacial interaction between them.

Fig. 2a shows the XRD patterns of g-C_3N_4 and BiOCl/g-C_3N_4 composites with different molar ratios. The pure g-C_3N_4 sample exhibited two diffraction peaks, where 2θ located at 12.86° corresponds to the (100) crystal plane diffraction of g-C_3N_4 and thus confirms the planar stacking structure of the triazine ring in the g-C_3N_4 lamellae [38]. The diffraction peak with 2θ located at 27.46° resulted from an interlayer stacking reflection specific to the conjugated aromatic system, which is related to the (002) crystal plane diffraction [32]. The diffraction peaks of BiOCl/g-C_3N_4 appeared prominently at 2θ values of 26.16°, 32.93°, 41.20°, 47.09°, 54.62° and 59.05°, corresponding to the (101), (102), (112), (200), (211) and (212) crystal planes of BiOCl (JCPDS cards No. 06-0249). According to Table S1 (Supporting information), with the increase in the proportion of g-C_3N_4, the grain size of the BiOCl/g-C_3N_4 composite initially increases and then decreases. This phenomenon may be attributed to the impact of increased nitrogen doping ratio on the crystal growth of BiOCl. When the proportion of g-C_3N_4 in the composite heterojunction increased, the diffraction peak attributed to g-C_3N_4 (2θ of 27.46°) gradually increased while the diffraction peak attributed to BiOCl gradually decreased, which suggests the successful synthesis of the BiOCl/g-C_3N_4 composite catalysts (enlarged figure) [39].

Fig. 2b illustrated the changes of surface functional groups in the BiOCl/g-C_3N_4 composite catalysts for different g-C_3N_4 ratios. For g-C_3N_4, the peak at 809 cm^{-1} results from the characteristic vibration mode of the ultrathin g-C_3N_4 tris-triazine units [37]. The wide peaks at 3000∼3300 cm^{-1} were the stretching vibration peak of the N–H bond. In addition, peaks in the range 1200–1650 cm^{-1} were representative stretching modes for CN heterocycles, such as peaks at 1237, 1316, 1406 and 1573 cm^{-1} for C–N stretching vibrations and 1640 cm^{-1} for C=N stretching vibrations, respectively [34]. In addition, the vibrational peak at 545.7 cm^{-1} was attributed

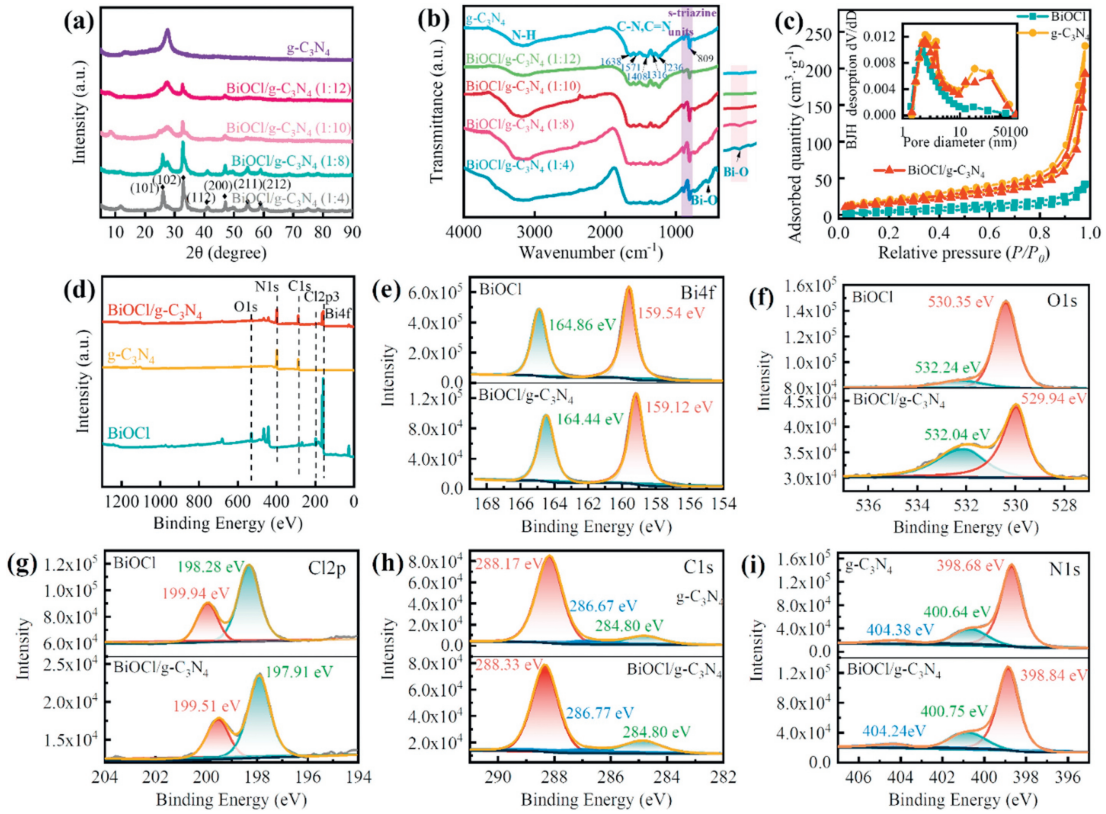

Fig. 2. (a) XRD patterns and (b) FTIR spectra of g-C_3N_4 and BiOCl/g-C_3N_4 samples with different molar ratios. (c) N_2 adsorption–desorption curves, pore diameter distribution curve (inset), (d) XPS surveys, (e) Bi 4f, (f) O 1s, (g) Cl 2p, (h) C 1s and (i) N 1s peaks of BiOCl, g-C_3N_4 and BiOCl/ g-C_3N_4.

to the Bi-O bond in BiOCl/g-C_3N_4 composite catalysts [39]. In the prepared BiOCl/g-C_3N_4 nanocomposites, the peaks of g-C_3N_4 and BiOCl coexist and no other new phases were observed. As the mass ratio of g-C_3N_4 in the composites increased, the peak intensity of g-C_3N_4 enhanced, while the peak intensity of BiOCl gradually decreased, which agrees with the XRD results.

The pore diameter distribution and specific surface area of BiOCl, g-C_3N_4 and BiOCl/g-C_3N_4 photocatalysts were determined by BJH method based on N_2 adsorption-desorption curves. The type IV isotherm and the type-H3 adsorption hysteresis loop in the high P/P_0 range were seen in Fig. 2c, indicating that all catalyst particles were mesoporous structure. The specific surface areas of the BiOCl, g-C_3N_4 and BiOCl/g-C_3N_4 catalysts were 13.94, 55.00 and 61.92 m^2/g, respectively. Apparently, after the combination of BiOCl with g-C_3N_4, the specific surface area of the composite was slightly improved. Most of the pore diameters of BiOCl catalyst particles were distributed in the range of 2–10 nm and were mesoporous structures. The pore diameter of g-C_3N_4 particles was mainly in the range of 2–10 nm and 10–50 nm, which was also mainly mesoporous structure, with a small portion of macroporous structure (>50 nm) (inset figure).

XPS technology was used to further explore the chemical states of the catalysts and the synthesis of heterojunctions. In Fig. 2d, five elements Bi, O, Cl, C and N were present in the composite BiOCl/g-C_3N_4 catalysts, which further proved the successful synthesis of the composite catalyst. The binding energy peak of Bi 4f was 164.44 eV and 159.12 eV belongs to Bi $4f_{5/2}$ and Bi $4f_{7/2}$, respectively, which is the characteristic of Bi^{3+} in BiOCl materials (Fig. 2e). The binding energy peak of O 1s at 532.04 eV and 529.94 eV is the oxygen vacancy in the catalyst and the Bi–O bond in the BiOCl crystal structure, respectively (Fig. 2f). Obviously, the content of oxygen vacancy in the BiOCl/g-C_3N_4 composite catalyst is higher than that of pure BiOCl. Two resolved peaks of Cl 1s were located at 199.51 and 197.91 eV, belonging to and Cl $2p_{1/2}$ and Cl $2p_{3/2}$, respectively (Fig. 2g) [31]. The binding energy peaks of C 1s at 284.8 eV, 286.77 eV and 288.33 eV belong to the sp^2 C–C or amorphous C–C, sp^3 C–$(N)_3$ and sp^2 N–C=N in the aromatic ring of g-C_3N_4 (Fig. 2h). The three resolved peaks of N 1s located at 404.24 eV, 400.75 eV and 398.84 eV belong to free amino groups C–N–H, sp^3 bridging N atoms of N–$(C)_3$ groups and sp^2 hybridized nitrogen of C–N=C (Fig. 2i). By comparing the high resolution XPS spectra of each element, it can be seen that the peaks of Bi 4f, O 1s and Cl 2p in BiOCl all move forward to the lower binding energy position after the combination with g-C_3N_4 [39]. In contrast, both C 1s and N 1s peaks in g-C_3N_4 move forward towards higher binding energy positions. These results demonstrated the existence of strong electron transfer between BiOCl and g-C_3N_4 in the complex, thus confirming the successful construction of the BiOCl/g-C_3N_4 heterojunction.

The effects of different molar ratios of g-C_3N_4 to BiOCl on the SMZ removal rate and the corresponding reaction kinetics under simulated solar light were first examined. Figs. 3a and b and Table S2 (Supporting information) show that the highest degradation rate (84.94%) of SMZ was achieved in 80 min when the molar ratio of g-C_3N_4 to BiOCl was 8:1, which yielded the highest reaction rate constant was 6.8×10^{-3} L mg^{-1} min^{-1}. The removal rates of SMZ were 81.13%, 83.21% and 81.79% when the molar ratio of BiOCl/g-C_3N_4 composite photocatalyst was 1:4, 1:10 and 1:12, respectively. Clearly, the proper molar ratio of BiOCl and g-C_3N_4 (*e.g.*, 8:1) is important for heterojunctions and photocatalytic properties. Excessive g-C_3N_4 could cause rapid recombination of the photoproduced e^--h^+ pares [39].

The dosage effect of BiOCl/g-C_3N_4 composite catalyst on SMZ removal rate and reaction kinetics is compared in Figs. 3c and d. As the catalyst dosage increased from 0.2 g/L to 0.8 g/L, the SMZ removal rate increased gradually from 89.22% to 92.77%, and the re-

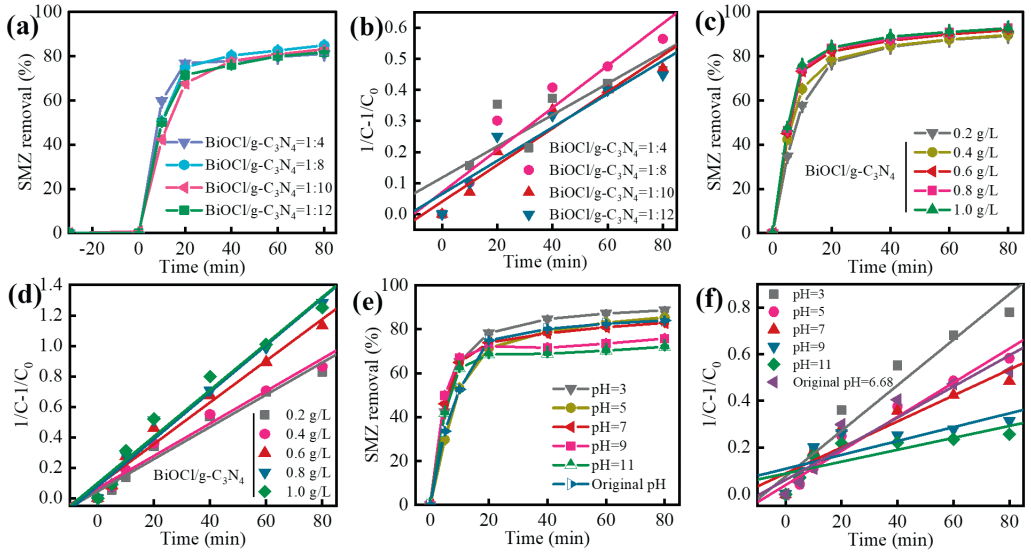

Fig. 3. The effects of (a, b) different molar ratios of g-C_3N_4 to BiOCl, (c, d) the initial concentration of BiOCl/g-C_3N_4 and (e, f) pH on the SMZ removal and *pseudo*-second-order kinetics under simulated solar light.

action rate increased from 1.05×10^{-2} to 1.54×10^{-2} L mg^{-1} min^{-1} as summarized in Table S3 (Supporting information). The slow increase in removal rate when the catalyst dosage was increased to 0.8 g/L was attributed to the scavenging effect of excess catalyst [40]. In addition, when the concentration of the catalyst was excessive, the solution was too turbid to prevent simulated solar light from passing through the reaction solution and thus the BiOCl/g-C_3N_4 photocatalyst could not effectively absorb the photon energy for the SMZ degradation [41]. Moreover, the excess catalyst would agglomerate in the aqueous phase, thus reducing the active sites on the surface, which would also reduce the photocatalytic efficiency of the catalyst [34]. In summary, in this photocatalytic system, the reaction conditions were established with a ratio of 1:8 between BiOCl and g-C_3N_4, and a catalyst dosage of 0.6 g/L.

The pH value in the aqueous medium significantly affects the adsorption rate of sulfamerazine on the BiOCl/g-C_3N_4 catalyst as both the speciation of sulfamerazine and the surface charge of BiOCl/g-C_3N_4. At the different initial pHs of the reaction solution (*e.g.*, 6.68, 3, 5, 7, 9 and 11), the removal efficiency of SMZ and the corresponding reaction kinetics were different as shown in Figs. 3e and f and Table S4 (Supporting information). The photocatalytic activity was higher under strongly acidic conditions with the degradation rate increased by 4.6% compared with the pH of 6.68. However, the alkaline condition reduced the degradation rate of SMZ by 12%. At acidic pHs, the BiOCl/g-C_3N_4 photocatalysts had a positive surface charge and the SMZ ($pK_{a,1}$, 2.56) was mainly in the form of anions, which caused strong electrostatic adsorption between the catalyst and SMZ and thus promoted the degradation of SMZ. When the pH was greater than 7.4 ($pK_{a,2}$), the photocatalytic degradation rate decreased due to the strong repulsive force between the surface of photocatalysts and SMZ [42].

The reusability and stability of the catalysts were examined using five consecutive photocatalytic cycling experiments under the same experimental conditions as shown in Fig. 4. Fig. 4a shows the degradation rate of SMZ was always above 80% after 5 cycles. Fig. 4b shows the XRD patterns of BiOCl/g-C_3N_4 before and after the repeated use. None of the characteristic peaks of the catalysts after reuse were shifted, indicative of no major changes in the crystal structures for BiOCl/g-C_3N_4. The FTIR spectra of BiOCl/g-C_3N_4 before and after use in Fig. 4c also reveal no changes of the functional groups on the BiOCl/g-C_3N_4 catalysts. Similarly, there were no significant changes in the XPS surveys before and after catalyst

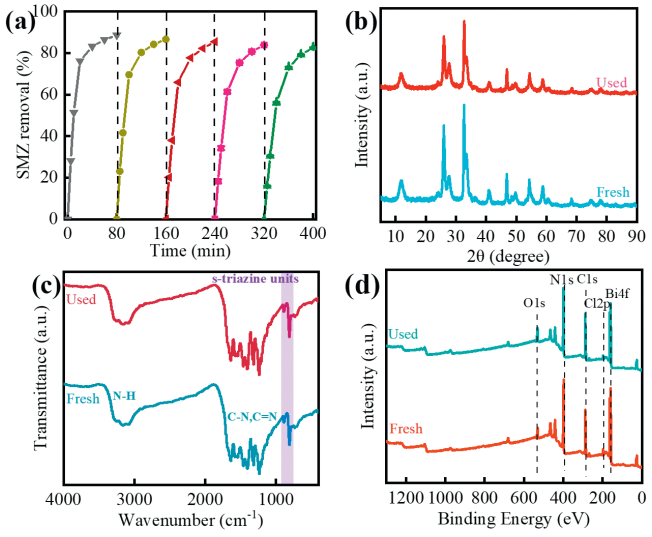

Fig. 4. (a) SMZ degradation curve during the five repeated experiments. The comparison of (b) XRD, (c) FTIR and (d) XPS surveys of the used and fresh BiOCl/g-C_3N_4 catalysts.

use (Fig. 4d). The photocatalytic performance and stability changes were probably attributed to photo-corrosion and metal leaching (Fig. S2 in Supporting information) [37].

To qualitatively analyze the dominant active species during the BiOCl/g-C_3N_4 catalyst photocatalytic reaction, isopropyl alcohol (IPA), KI and *p*-benzoquinone (BQ) were used as scavengers of hydroxyl radical ($^{\bullet}OH$), electron-hole (h^+) and superoxide anion ($^{\bullet}O_2^-$), respectively [28,43]. Figs. 5a and b shows the presence of each scavenger inhibited the degradation of SMZ, which decreased from 1.37×10^{-2} L mg^{-1} min^{-1} to 1.03×10^{-2} L mg^{-1} min^{-1}, 0.78×10^{-2} L mg^{-1} min^{-1} and 0.94×10^{-2} L mg^{-1} min^{-1}, respectively, after the addition of IPA, KI and BQ to the reaction system. Thus, the h^+ played a major role in this photocatalytic reaction as indicated by the strongest inhibition from KI. The inhibition of BQ ranked second, indicating that the $^{\bullet}O_2^-$ radical played a secondary role in the reaction.

The active species in the photocatalytic system were further detected by ESR under no light and simulated solar light irradiation.

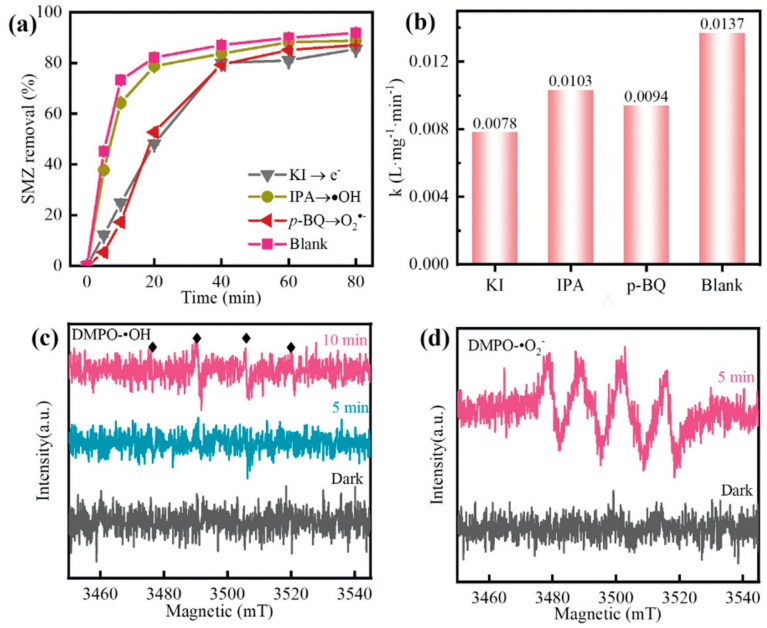

Fig. 5. (a) The removal efficiency of SMZ by BiOCl/g-C_3N_4 photocatalysts in different scavengers under simulated solar light irradiation and (b) the corresponding apparent rate constants. ESR spectra of (c) DMPO-$^{\bullet}$OH and (d) DMPO-$^{\bullet}O_2^-$.

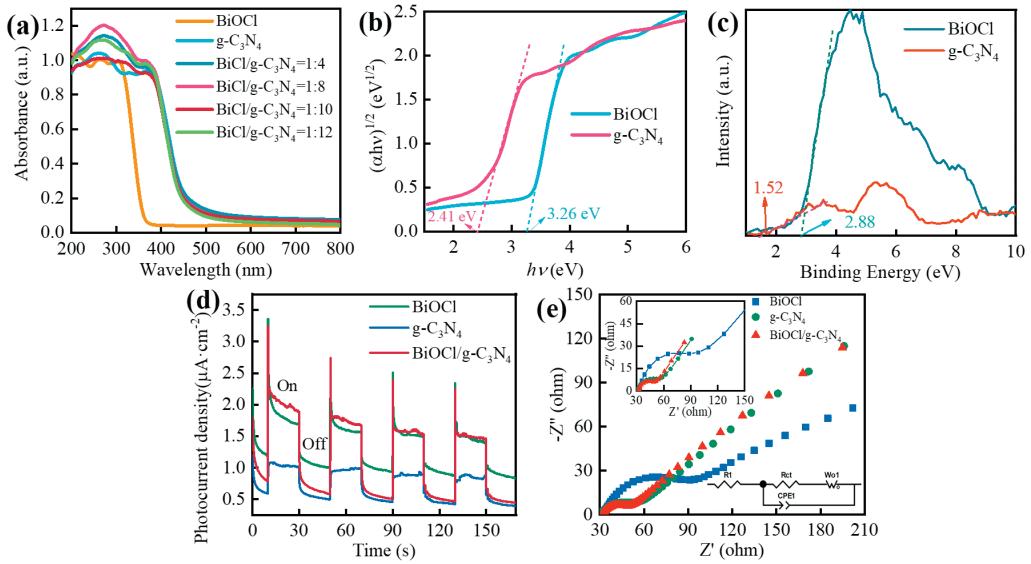

Fig. 6. (a) The UV–vis diffuse reflectance spectra. (b) Tauc plots and (c) VB-XPS of obtained catalysts. (d) The photocurrent responses (*i-t* curves) and (e) EIS spectra of BiOCl, g-C_3N_4 and BiOCl/g-C_3N_4 composite catalysts.

Figs. 5c and d shows no signals of DMPO-$^{\bullet}$OH and DMPO-$^{\bullet}O_2^-$ adducts in the dark environment. Under simulated solar light irradiation, the characteristic quadruplet signal with a peak height ratio of 1:2:2:1 indicated the presence of DMPO-$^{\bullet}$OH adducts, while the four peaks with relative intensities of 1:1:1:1 corresponded to DMPO-$^{\bullet}O_2^-$ adducts. In addition, the signal intensity of DMPO-$^{\bullet}$OH, although very weak, was enhanced with the irradiation time. In contrast, the signal intensity of DMPO-$^{\bullet}O_2^-$ was strengthened quite significantly with the prolongation of irradiation time. Therefore, the BiOCl/g-C_3N_4 catalyst could generate h^+, $^{\bullet}$OH and $^{\bullet}O_2^-$ under simulated solar light irradiation, while h^+ was the primary reactive species in the degradation of SMZ.

UV–vis DRS in Fig. 6a was used to examine the optical properties of the catalysts. The absorption edge of BiOCl is in the UV region, while it is red-shifted after composite with g-C_3N_4. For semiconductor materials, the band gap (E_g) can be calculated by the equation $\alpha h\nu = A(h\nu - E_g)^{n/2}$, where α is the absorption coefficient, h is Planck's constant, ν is the optical frequency, and A is a constant. The n value is determined by the type of semiconductor leap, and since both BiOCl and g-C_3N_4 are indirect semiconductors, n is taken as 4. Fig. 6b shows the band gap of BiOCl and g-C_3N_4 are 3.26 eV and 2.41 eV, respectively. The VB-XPS (valence band-XPS) of the samples can be seen in Fig. 6c, VB-XPS of BiOCl and g-C_3N_4 are 2.88 eV and 1.52 eV, respectively. The E_{VB} for the corresponding standard hydrogen electrode ($E_{VB,\ NHE}$) can be computed using the equation: $E_{VB,\ NHE} = \varphi + E_{VB,\ XPS} - 4.44$, where φ represents the instrument's work function (4.2 eV) [44]. Thus, the VB of the BiOCl and g-C_3N_4 are 2.64 eV and 1.28 eV. The

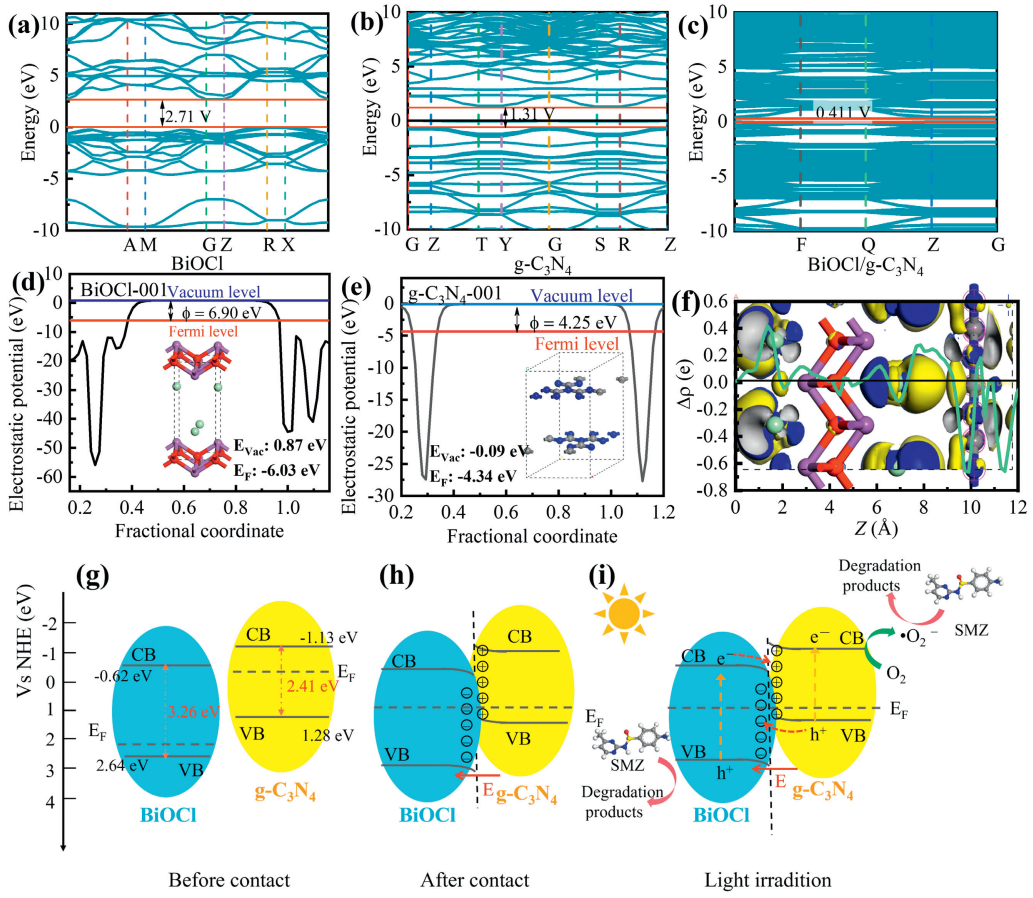

Fig. 7. The band structure of (a) BiOCl, (b) g-C_3N_4 and (c) BiOCl/g-C_3N_4. The calculated work function of (d) BiOCl and (e) g-C_3N_4. (f) The 3D charge density difference and planar-averaged electron density difference. (g-i) The proposed photocatalytic mechanism for the degradation of SMZ by BiOCl/g-C_3N_4 heterojunction.

corresponding conduction band (CB) positions of the BiOCl and g-C_3N_4 are calculated to be −0.62 eV and −1.13 eV, respectively, according to the formula $E_{CB} = E_{VB} - E_g$.

In order to explore the efficiency of photogenerated carrier separation of the catalysts, photoelectric chemical detection technology was used. In Fig. 6d, each catalysts exhibited fast response to the light source being turned on or off and showed significant photocurrent decay under light irradiation, which implies rapid recombination of light-generated electrons and holes. The photocurrent response values of the BiOCl/g-C_3N_4 heterojunctions were significantly higher than those of the BiOCl and g-C_3N_4 catalysts, which further demonstrates the excellent carrier separation efficiency of BiOCl/g-C_3N_4 heterojunction. The electrochemical impedance spectroscopy (EIS spectra) showed that the radius of BiOCl/g-C_3N_4 was smallest (Fig. 6e). The EIS spectra depicted in Fig. 6e were modeled using an equivalent circuit diagram (inset). The charge-transfer resistances (R_{ct}) values for BiOCl, g-C_3N_4, and BiOCl/g-C_3N_4 were determined as 56.39 Ω, 24.19 Ω, and 18.7 Ω, respectively, indicating the fastest photo-induced electron-hole pair transfer and separation efficacy under simulated solar light irradiation, and thus the excellent photocatalytic activity of BiOCl/g-C_3N_4.

To further investigate the mechanism of the heterojunction formed by BiOCl/g-C_3N_4, a quantum mechanical simulation analysis was conducted. After the crystal structure models of BiOCl and g-C_3N_4 were optimized (Fig. S1 in Supporting information), the energy band structures were calculated separately and shown in Figs. 7a and b. The Fermi levels of both BiOCl and g-C_3N_4 were located at 0 eV, and the conduction band and valence band were located below and above the Fermi level, respectively. The bottom of the conduction band and the top of the valence band were located at different high symmetry points (K points), which confirmed that both BiOCl and g-C_3N_4 were indirect semiconductor structures [39]. The calculated band gaps were 2.71 and 1.31 eV, respectively, which were smaller than the experimentally measured results, which is commonly observed in GGA and local-density approximation (LDA) calculations [45]. Fig. 7c indicates the BiOCl/g-C_3N_4 composite's energy band structure was denser than their separate forms. The high electron density is helpful for the production of more photogenerated carriers.

To further explore the photocatalytic mechanism of BiOCl/g-C_3N_4, the Fermi energy level of each catalyst was determined by calculating their work functions [46]. Figs. 7d and e show the Fermi energy levels of BiOCl and g-C_3N_4 were 6.90 eV and 4.25 eV, respectively, indicative of the potential electron transfer from g-C_3N_4 to BiOCl at the contact interface. Additionally, the three-dimensional charge density difference and the planar average electron density difference in Fig. 7f were used to detect the charge transfer and depletion in the composites. The yellow region indicates charge depletion and the blue region indicates charge accumulation. The charge accumulation mainly occurs in the upper region of BiOCl in Fig. 7f, while the charge depletion mainly occurs in the lower region of g-C_3N_4, indicating the charge transfer in the BiOCl/g-C_3N_4 heterojunction from g-C_3N_4 to BiOCl. The difference in the average charge density in the z-direction indicates charge depletion and accumulation in Fig. 7f (green line), with positive and negative indicating charge accumulation and depletion, respectively.

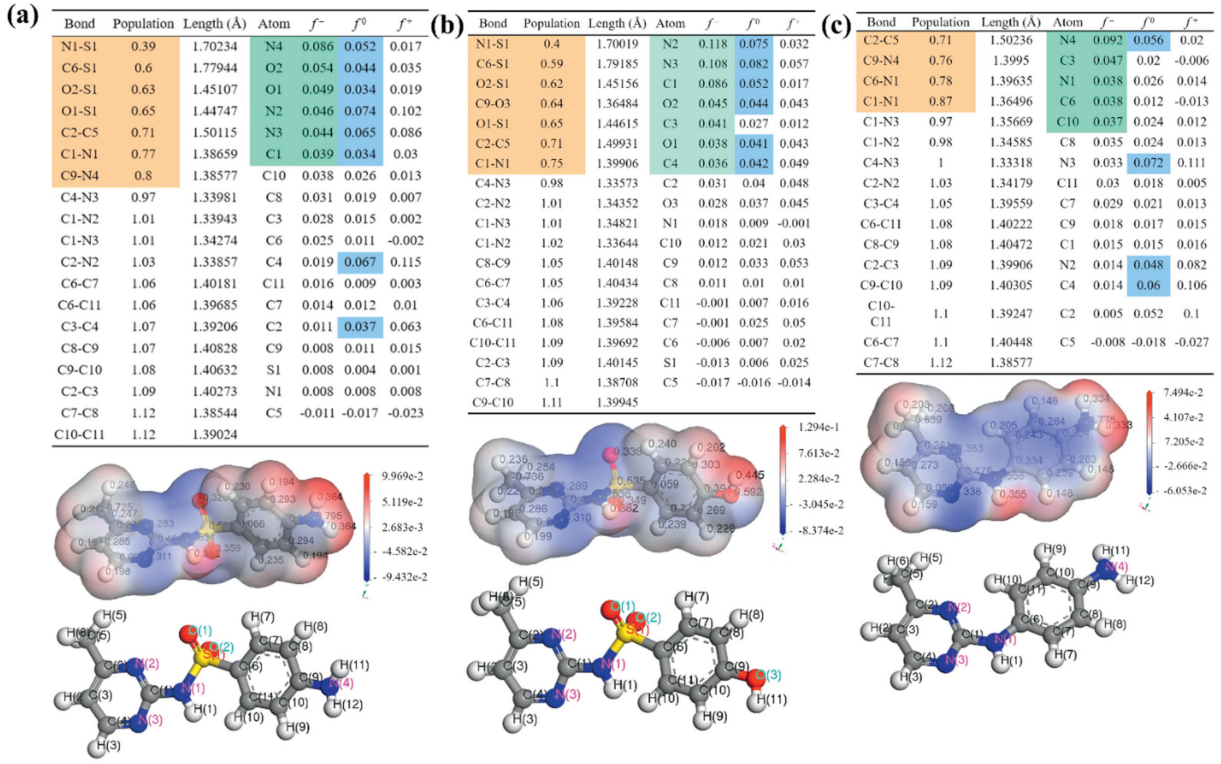

Fig. 8. The bond population, Fukui indices and electrostatic potential distribution of (a) SMZ, (b) **P1**, and (c) **P2**.

Based on the above analysis, the photocatalytic mechanism for the degradation of SMZ by BiOCl/g-C_3N_4 heterojunction was proposed in Figs. 7g–i. Upon contact between the two photocatalysts, the electrons transferred from g-C_3N_4 with a lower Fermi energy level to BiOCl with a higher Fermi energy level. As a result, g-C_3N_4 became positively charged. On the contrary, BiOCl was negatively charged. In addition, upward or downward band bending occurred at the g-C_3N_4 and BiOCl interfaces, respectively. An internal electric field pointing from g-C_3N_4 to BiOCl was also formed [47]. Under light irradiation, the photogenerated electrons were produced and transferred from the conduction band of BiOCl to the valence band of the g-C_3N_4. In addition, the Coulombic gravitational force, the energy band bending between the electrons in the BiOCl and the holes in the g-C_3N_4 also facilitated the charge transfer. Hence, the stronger photogenerated e^- retained in the conduction band of g-C_3N_4 reacted with the dissolved O_2 in water to form $^{\bullet}O_2^-$, while the photogenerated holes retained in the valence band of BiOCl reacted with H_2O and $^{\bullet}O_2^-$ to form respectively $^{\bullet}OH$. Finally, the above generated photogenerated h^+, $^{\bullet}O_2^-$ and $^{\bullet}OH$ migrated to the surface of the photocatalysts to degrade the SMZ into the small-molecule intermediates or inorganic species such as CO_2 and H_2O.

After photocatalytic reaction, the SMZ mineralization rate was 26.26%. The degradation pathways of SMZ were predicted by HPLC-QTOF-MS/MS and DFT calculations [4,5,48]. As can be seen from Fig. S3 and Table S5 (Supporting information), a total of 13 intermediate products of SMZ were detected. Fig. 8 shows the molecular structure models, populations and lengths of bonds, Fukui indices (f^-, f^0, f^+) of the atoms and electrostatic potential distribution for the two main degradation products of SMZ and SMZ, respectively. The predicted degradation pathway in Fig. 9a in the photocatalytic system of BiOCl/g-C_3N_4 indicates that h^+ as the major active species enabled electrophilic reactions, followed by free radical reactions and nucleophilic reactions. The smaller the population of a chemical bond, the weaker it was and the more likely it was to break [49]. The larger the Fukui indices of an atom, the more vulnerable it was to attack [50]. As shown in Fig. 8a, based on the populations, the N1-S1, C6-S1, O2-S1, O1-S1, C2-C5, C1-N1 and C9-N4 were weak and prone to break. While N4, O2, O1, N2, N3 and C1 were easily attacked by active species. Therefore, intermediate products such as **P1**, **P2**, **P3**, **P4**, **P5**, **P6**, **P7**, **P8**, and **P9** might be produced after the photocatalytic degradation of SMZ through deamination hydroxylation, SO_2 extrusion and breaking bonds (Fig. 9a). Similarly, the populations of N1-S1, C6-S1, C9-O3, O2-S1, C2-C5 and C1-N1 in **P1** were smaller (Fig. 8b). And the Fukui indices (f^-, f^0) of N2, N3, C1, O2, C3, O1 and C4 were larger, suggesting the generation of **P6**, **P7**, **P10**, **P10**, **P11** (Fig. 9a). As shown in Fig. 8c, C2-C5, C9-N4, C6-N1 and C1-N1 in **P2** were the weakest bonds, while the N4, C3, N1, C6 and C10 atoms were vulnerable to attack, resulting in the generation of **P6**, **P7**, **P11** and **P13** (Fig. 9a). Eventually, all intermediates obtained continue to be oxidized to inorganic small molecules such as CO_2 and H_2O.

Ecological structure activity relationships (ECOSAR) software was used to predict the toxicity of SMZ and its intermediates during photocatalytic degradation by adopting quantitative structure-activity relationship (QSAR), and the results were shown in Fig. 9b. The predicted toxicity indicators were the Green Algal half-maximum effect concentration (EC_{50}), the Daphnid half lethal concentration (LC_{50}, 48 h) and the fish LC_{50} (48 h) and their corresponding chronic value (Chv). In conclusion, during the photocatalytic degradation of SMZ over BiOCl/g-C_3N_4 heterojunction catalysts under simulated solar light, the ecotoxicity of the intermediate products of SMZ was reduced, which was of practical significance for the removal of SMZ from wastewater.

The g-C_3N_4-based catalysts are considered as classical visible light responsive photocatalysts, and other catalysts used for photocatalytic oxidation of SMZ are summarized in Table 1 [15,16,42,51,52]. Although catalysts such as TiO_2 and ZnO were modified to yield moderate photocatalytic activity under visible light. The g-C_3N_4 catalysts can improve their photocatalytic performance through complex morphological modifications, but the

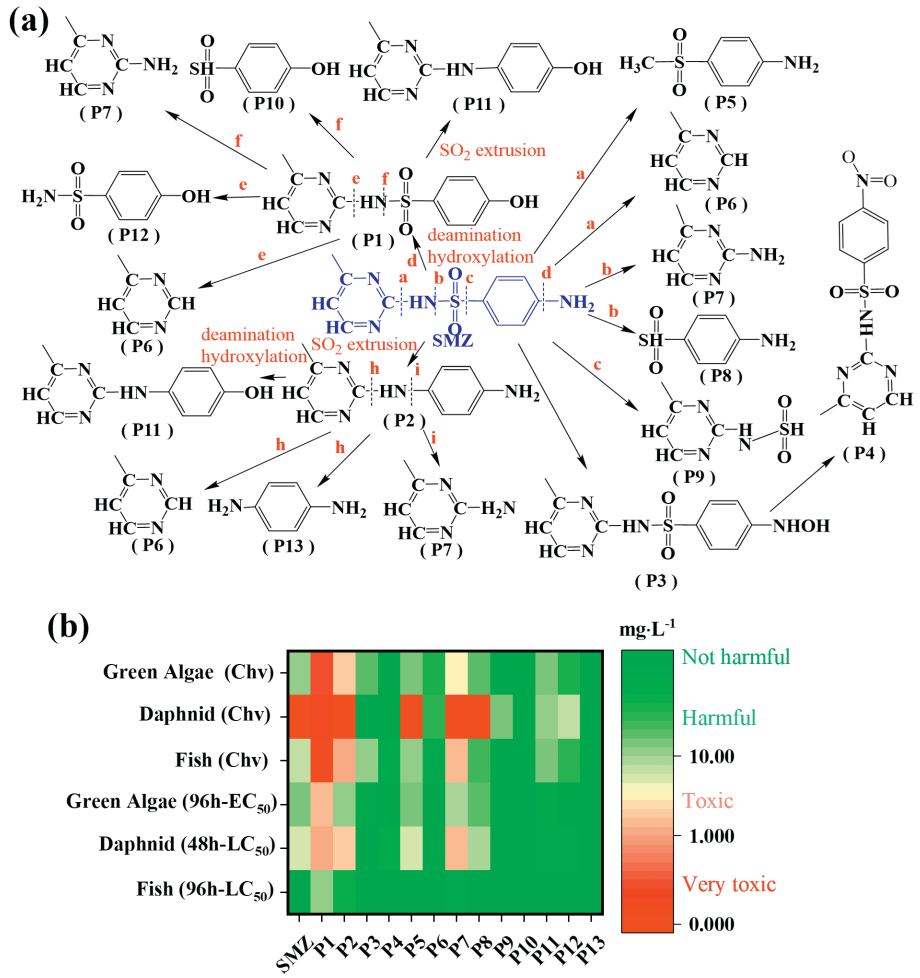

Fig. 9. (a) The predicted degradation pathway of SMZ in BiOCl/g-C_3N_4 photocatalytic system. (b) Toxicity value of SMZ and its possible degradation intermediates.

Table 1
Comparison with other literature about SMZ degradation in photocatalytic system.

Photocatalysts	Photocatalysts concentration (g/L)	Sulfamerazine concentration (mg/L)	Nature of lamp	Reaction time (min)	Removal rate (%)	Ref.
Cu-TiO_2@functionalized SWCNT	0.9	30	Xenon lamp	135	100	[42]
Distorted g-C_3N_4	1.0	10	Xenon lamp	60	99	[51]
Pd/Bi_2MoO_6/g-C_3N_4	0.5	5	LED lamps	90	98.8	[52]
La-MIL-53(Al)/ZnO	0.5	20	Xenon lamp	120	92	[16]
Bi-TiO_2	1.0	20	Xenon lamp	300	81.18	[15]
BiOCl/g-C_3N_4	0.8	10	Xenon lamp	80	92.77	This work

BiOCl/g-C_3N_4 heterojunction shows significant advantages in enhancing reaction kinetics of SMZ and perhaps other refractory organic pollutants in wastewater treatment.

In this work, BiOCl/g-C_3N_4 heterojunction was prepared by one-step direct precipitation and achieved 92.77% of SMZ within 80 min under simulated solar light. The catalyst also showed excellent chemical stability in the recovery experiments. The formation of an inner electric field and carrier transfer through the S-scheme heterojunction formed at the interface of BiOCl and g-C_3N_4, resulting in the generation of a large number of reactive species and the rapid degradation of SMZ, which was proven by photoelectrochemical tests and DFT calculation. DFT calculations also predicted the attack sites of free radicals and the possible photocatalytic degradation pathways of SMZ. This study offers a facile and effective synthesis of BiOCl/g-C_3N_4 photocatalysts for the degradation of SMZ in wastewater.

Declaration of competing interest

The authors declare that they have no known competing financial interests or personal relationships that could have appeared to influence the work reported in this paper.

Acknowledgments

The work was supported by the National Natural Science Foundation of China (No. 52370174), the Natural Science Foundation of Shandong Province, China (No. ZR2022ME128), Special Projects in Key Areas of Colleges and Universities in Guangdong Province (No. 2023ZDZX4050), and Talents of High-Level Scientific Research Foundation of Qingdao Agricultural University (No. 6651120004).

Supplementary materials

Supplementary material associated with this article can be found, in the online version, at doi:10.1016/j.cclet.2024.109767.

References

[1] X. Liu, H. Ji, S. Li, et al., Chemosphere 233 (2019) 198–206.
[2] T. Shen, X. Wang, J. Li, et al., Appl. Catal. B: Environ. 328 (2023) 122518.
[3] Y. Yao, N. Mi, Y. Zhu, et al., RSC Adv. 9 (2019) 9145–9152.
[4] Y. Liu, N. Tan, J. Guo, et al., J. Hazard. Mater. 396 (2020) 122751.
[5] A. Bahadoran, S. Ramakrishna, S. Masudy-Panah, et al., Appl. Surf. Sci. 568 (2021) 150957.
[6] C. Yan, Y. Yang, J. Zhou, et al., Environ. Pollut. 175 (2013) 22–29.
[7] W. Kong, Q. Yue, Y. Gao, et al., Chem. Eng. J. 413 (2021) 127456.
[8] Y. Yang, W. Song, H. Lin, et al., Environ. Int. 116 (2018) 60–73.
[9] Z. Ouyang, C. Yang, J. He, et al., Chem. Eng. J. 402 (2020) 126122.
[10] L. Qin, X. Pang, H. Zeng, et al., Sci. Total Environ. 708 (2020) 134552.
[11] S. Zhuang, Y. Liu, J. Wang, J. Hazard. Mater. 383 (2020) 121126.
[12] P. Gao, X. Chen, M. Hao, et al., Chemosphere 228 (2019) 521–527.
[13] Y. Zhao, Y. Li, L. Sun, Chemosphere 276 (2021) 130201.
[14] M.I. Din, R. Khalid, J. Najeeb, et al., J. Clean. Prod. 298 (2021) 126567.
[15] N. Wang, X. Li, Y. Yang, et al., Sep. Purif. Technol. 211 (2019) 673–683.
[16] Q. Wei, W. Li, C. Jin, et al., J. Rare Earths 40 (2022) 595–604.
[17] C. Ma, J. Wei, K. Jiang, et al., Sci. Total Environ. 855 (2023) 158644.
[18] L. Yao, H. Yang, Z. Chen, et al., Chemosphere 273 (2021) 128576.
[19] J. Li, Z. Zhao, Z. Li, et al., Chin. Chem. Lett. 33 (2022) 3705–3708.
[20] J. Guo, X. Li, J. Liang, et al., Coord. Chem. Rev. 443 (2021) 214033.
[21] Y. Yang, C. Zhang, C. Lai, et al., Adv. Colloid. Interface. Sci. 254 (2018) 76–93.
[22] X. Yang, S. Sun, L. Ye, et al., Sep. Purif. Technol. 299 (2022) 121725.
[23] S. Tao, S. Sun, T. Zhao, et al., Appl. Surf. Sci. 543 (2021) 148798.
[24] Y. Lu, J. Song, W. Li, et al., Appl. Surf. Sci. 506 (2020) 145000.
[25] A. Kumar, A. Kumar, G. Sharma, et al., Chem. Eng. J. 334 (2018) 462–478.
[26] Z. Cirena, Y. Nie, Y. Li, et al., Chin. Chem. Lett. 34 (2023) 107726.
[27] D. Huang, X. Sun, Y. Liu, et al., Chin. Chem. Lett. 32 (2021) 2787–2791.
[28] G. Zhao, J. Ding, F. Zhou, et al., Chem. Eng. J. 405 (2021) 126704.
[29] J. Wang, L. Tang, G. Zeng, et al., Appl. Catal. B: Environ. 209 (2017) 285–294.
[30] K. Dou, C. Peng, R. Wang, et al., Chem. Eng. J. 455 (2023) 140813.
[31] X. Wang, Q. Wang, F. Li, et al., Chem. Eng. J. 234 (2013) 361–371.
[32] Y. Bai, P. Wang, J. Liu, et al., RSC Adv. 4 (2014) 19456–19461.
[33] X. Zhang, T. Guo, X. Wang, et al., Appl. Catal. B: Environ. 150-151 (2014) 486–495.
[34] C. Yang, H. Chai, P. Xu, et al., Sep. Purif. Technol. 288 (2022) 120609.
[35] Q. Liu, W. Zhao, Z. Ao, et al., Chin. Chem. Lett. 33 (2022) 410–414.
[36] Y. Deng, S. Shu, N. Fang, et al., Chin. Chem. Lett. 34 (2023) 107323.
[37] Q. Wang, P. Wang, P. Xu, et al., Appl. Catal. B: Environ. 266 (2020) 118653.
[38] C. Yang, Z. Zhang, P. Wang, et al., J. Hazard. Mater. 451 (2023) 131154.
[39] Q. Wang, W. Wang, L. Zhong, et al., Appl. Catal. B: Environ. 220 (2018) 290–302.
[40] Y. Huang, C. Han, Y. Liu, et al., Appl. Catal. B: Environ. 221 (2018) 380–392.
[41] P. Xu, P. Wang, Q. Wang, et al., J. Hazard. Mater. 403 (2021) 124011.
[42] A. Payan, A. Akbar Isari, N. Gholizade, Chem. Eng. J. 361 (2019) 1121–1141.
[43] J. Qu, Z. Li, F. Bi, et al., Proc. Natl. Acad. Sci. U. S. A. 120 (2023) e1990415176.
[44] X. Li, B. Kang, F. Dong, et al., Nano Energy 81 (2021) 105671.
[45] J. Yang, J. Sun, S. Chen, et al., Sep. Purif. Technol. 290 (2022) 120881.
[46] W. Yao, J. Zhang, Y. Wang, et al., Appl. Surf. Sci. 435 (2018) 1351–1360.
[47] X. Zhang, Y. Song, X. Niu, et al., Appl. Catal. B: Environ. 342 (2024) 123445.
[48] M. Xie, M. Yao, S. Zhang, et al., Sep. Purif. Technol. 304 (2023) 122398.
[49] P. Xu, X. Li, R. Wei, et al., Chem. Eng. J. 462 (2023) 142204.
[50] P. Xu, R. Wei, P. Wang, et al., Water Res. 235 (2023) 119843.
[51] C. Zhou, G. Zeng, D. Huang, et al., J. Hazard. Mater. 386 (2020) 121947.
[52] G. Di, Z. Zhu, H. Zhang, et al., Chem. Eng. J. 401 (2020) 126061.